Journal of Structural Geology 23 (2001) 51–66

Controls on the failure mode of brittle inclusions hosted in a ductile matrix

Nibir Mandal[a], Chandan Chakraborty[b,*], Susanta Kumar Samanta[a]

[a]*Department of Geological Sciences, Jadavpur University, Calcutta 700032, India*
[b]*Geological Studies Unit, Indian Statistical Institute, 203 B.T. Road, Calcutta 700035, India*

Received 14 December 1999; accepted 17 July 2000

Abstract

Plane strain deformation experiments were performed on elliptical inclusions of cohesive sand embedded within a slab of pitch, with the aim of investigating the mode of fracturing of brittle inclusions within a ductile matrix. Under pure and simple shear, the inclusions failed in three different modes: tensile fracturing (Mode 1), shear fracturing (Mode 2a) and extensional shear fracturing (Mode 2b). Jeffrey's (1922) theory of the flow of a viscous medium around an ellipsoidal body was applied to the experimental results to determine the principal tensile and compressive stresses within an inclusion, and analyze the failure modes using Griffith's Criterion. The analysis reveals that the aspect ratio (R) and the orientation (θ) of the inclusion control the principal tensile and compressive stresses within it, and in turn govern the mode of brittle deformation. At a particular inclusion orientation, the tensile stress increases, whereas the compressive stress decreases monotonically with increasing aspect ratio of the inclusion. The principal stresses also vary with inclusion orientation for a given aspect ratio, but not monotonically. The analysis delimits the fields of each mode of brittle deformation of inclusions in R- θ space under pure shear and simple shear.

1. Introduction

A rock system containing stiff inclusions in a ductile matrix is mechanically analogous to fibre composites. The concept of fibre-loading theory (e.g. Cox, 1952) can thus be applied to understand fracturing of brittle inclusions (cf. Brittle Microtectonics, Hancock, 1985) floating in a ductile matrix in rocks (Mitra, 1978; Ramsay and Huber, 1987; Hippertt, 1993; Michibayashi, 1996; Ji et al., 1997). Ramberg (1955), in an attempt to analyze boudinage structures, extrapolated this kind of deformation mechanics to rock systems by considering a stiff elastic plate between two viscous layers. He suggested that the flowing ductile matrix exerts traction on the surface of the stiff inclusion, which in turn develops a tensile stress within the inclusion that leads to fracture when the tensile stress reaches the tensile strength of the material. Subsequently, several workers have developed this model in order to gain a better understanding of the *tensile fracturing* of brittle inclusions in rocks (Hobbs, 1967; Lloyd and Ferguson, 1981, Lloyd et al., 1982; Masuda and Kuriyama, 1988; Ji et al., 1997). However, an inventory of *intra-inclusion* fractures in rocks reveals that besides *tensile fractures* (hereafter called Mode 1), two other modes of fractures occur: *shear fractures* (hereafter called Mode 2a) and *extensional shear fractures* (hereafter called Mode 2b) (Fig. 1).

This paper presents results of analogue model experiments that were conducted to investigate the mode of failure of brittle inclusions in a ductile matrix. Since theoretical models of this phenomenon primarily focus on tensile failure, a theoretical analysis is developed to describe shear failure of the inclusions. This analysis is used to evaluate the geometric conditions (shape and orientation of the brittle inclusion) that favour the different modes of brittle failure of stiff inclusions embedded within a ductile material.

2. Analogue models

2.1. Experimental method

Experiments were performed on models containing elliptical inclusions of cohesive sand embedded within a slab of pitch (length 20 cm, width 15 cm and thickness 6 cm). The cohesive sand deformed in a brittle manner, while the pitch underwent ductile flow. Earlier workers have used loose, non-cohesive sand for modelling of large-scale fault structures (McClay and Ellis, 1987; Mulugeta, 1988; Huiqi et al., 1992; Mandal, et al., 1997). In our experiments we chose cohesive sand so that the sandy inclusion could rupture both by tensile and shear fractures.

* Corresponding author.
E-mail addresses: nibir@jugeo.cli0.ernet.in (N. Mandal), chandan@isical.ac.in (C. Chakraborty).

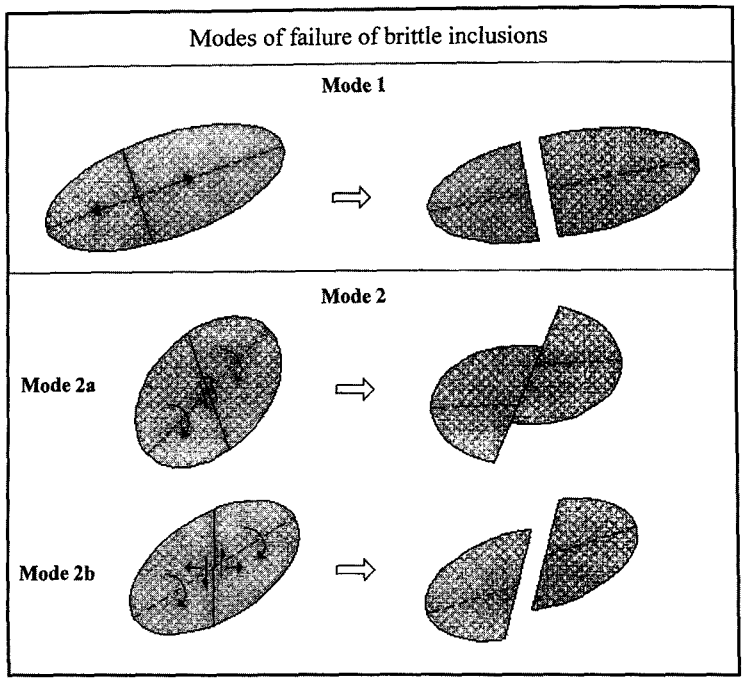

Fig. 1. Three modes of fracturing of rigid inclusion in a ductile matrix. Mode 1: failure by tensile fracturing. Mode 2a: failure by shear fracturing involving rotation and offsetting of the fragments. Mode 2b: failure by extensional shear fracturing involving rotation, offsetting and separation of the fragments.

The models were prepared in the following way. Dry, fine-grained (65–70 mesh) white sand and plaster-of-paris were mixed homogeneously in 10:1 volume ratio. Water was then added to the mixture to form a mortar like material. We prepared a 1-cm thick bed of this material on a glass plate, and allowed it to dry for a couple of minutes. A cylindrical portion with an elliptical cross-section was cut out from the bed. The inclusion was then embedded within a pitch slab. The final model of the pitch block had a flat top surface exposing the elliptical face of the inclusion (Fig. 2).

The model was placed on a glass plate and deformed under pure shear or simple shear by moving two parallel vertical bars (Fig. 2). Another glass plate was fixed at the top of the model to restrict flow of pitch in the vertical direction to achieve a plane strain condition. To minimize friction, the surfaces of the glass plates in contact with the pitch were smeared with liquid soap. The progressive deformation of the model was observed and photographed through the top glass plate.

2.2. *Modes of brittle inclusion failure: experimental observations*

2.2.1. *Pure shear*

A set of experiments was performed in pure shear with the long axis of the inclusion parallel to the bulk extension

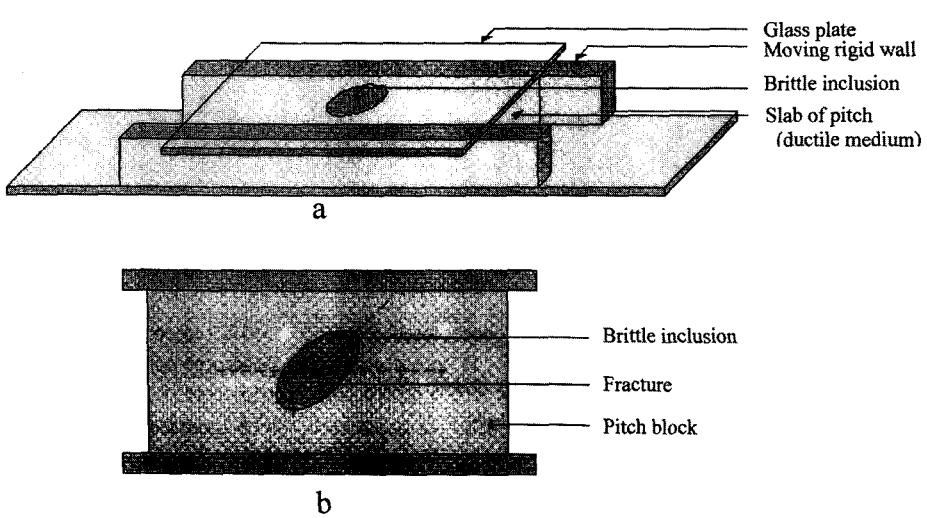

Fig. 2. Schematic three-dimensional (a) and plan (b) views of the experimental setup.

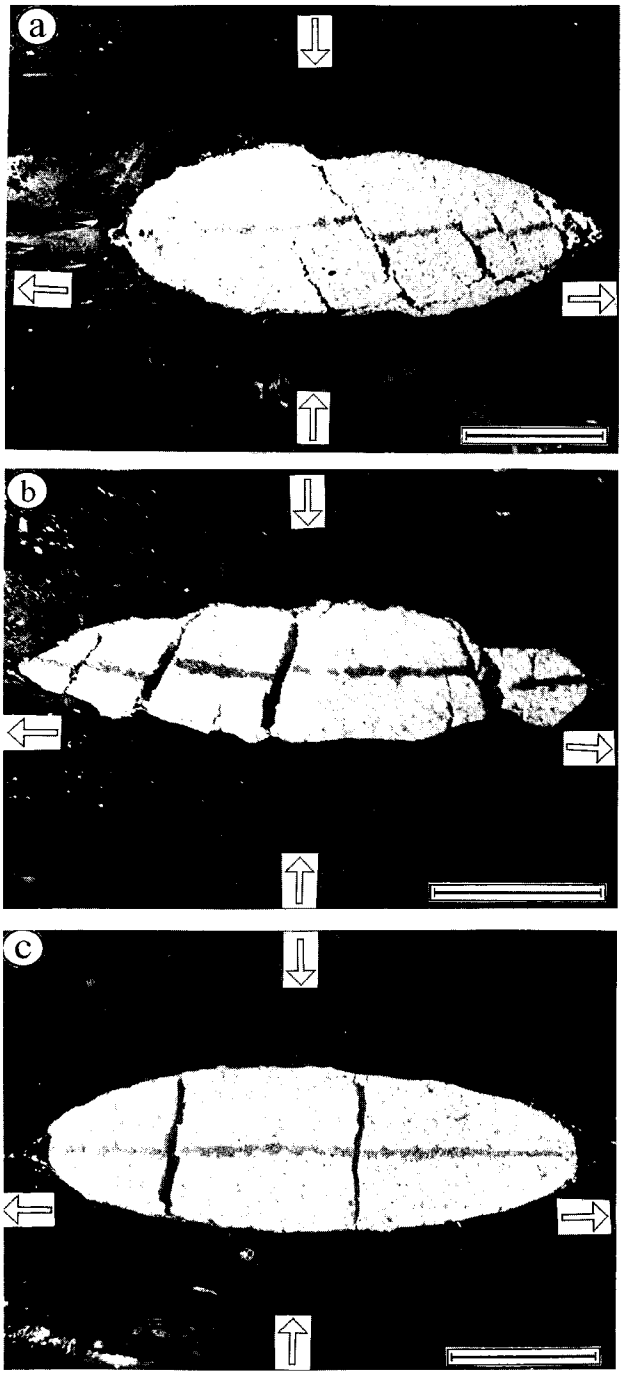

Fig. 3. Fracturing modes of the inclusions in the experiments during pure shear. (a) Mode 2a, (b) Mode 2b and (c) Mode 1. Aspect ratio = 1.9, 2.8 and 3 in (a), (b) and (c) respectively. The long axes of the inclusions were parallel to the bulk extension direction. Scale bars = 2 cm.

direction. When the aspect ratio of the inclusion was less than 1.2, the inclusion did not fracture at all, and remained intact throughout the progressive deformation. Inclusions with an aspect ratio of about 1.5 underwent failure by shear fracturing in Mode 2a, involving rotation and off-setting of the fragments (Fig. 3a). As the aspect ratio was further increased, this mode of deformation was replaced by Mode 2b (Fig. 3b). At aspect ratios of greater than 3.1, the mode of failure was by tensile fractures (Mode 1) at right angles to the long axis of the inclusion (Fig. 3c).

In another set of experiments, the long axis of brittle inclusion was set at an angle to the bulk extension direction. In these experiments the inclusions rotated towards the bulk extension direction during the deformation. Inclusions with a moderate aspect ratio ($R = 1.8$) and a long axis initially at an angle of 40° to the bulk extension direction did not fracture until they had rotated to an angle of about 20°, at which point Mode 2a shear fractures formed (Fig. 4a). The fractures were generally off-centred (Fig. 4a). For the same initial orientation, inclusions with an aspect ratio $R = 2.6$ ruptured in Mode 2b (Fig. 4b), and those with larger aspect ratios fractured in Mode 1 (Fig. 4c) after having rotated by a smaller amount than in the low aspect ratio model.

2.2.2. *Simple shear*

Another set of experiments was performed in simple shear. These experiments also showed contrasting modes of brittle deformation. Inclusions with a large aspect ratio ($R = 4$) and long axis initially at an angle close to 45° with the shear direction ruptured in Mode 1 immediately at the onset of deformation (Fig. 5a). In contrast, inclusions of the same aspect ratio, but with the long axis initially parallel to the shear direction did not rotate significantly during deformation and as a result did not rupture even after a large bulk shear. For moderate aspect ratios (about 2.6) the deformation took place either in Mode 1 or Mode 2, depending upon the initial orientation of the inclusion with respect to the shear direction. The inclusion ruptured in Mode 1 when the long axis was initially at an angle of 40° to the shear direction (Fig. 5b), but in Mode 2b when the initial orientation was 30° (Fig. 5c).

In summary the experimental results reveal that: 1) the inclusions do not rupture until their aspect ratio is larger than a critical value and they attain orientations with respect to the bulk extension and shear directions within a specific range during deformation; 2) the failure of brittle inclusions can occur in any of the three modes; 3) the mode of fracturing is sensitive to the aspect ratio and the orientation of the inclusions at the moment of fracturing; and 4) in some situations the tensile fractures may be oblique to the long axis of the inclusion and the bulk extension direction.

3. Theoretical analysis

Theoretical modelling of fracture development within brittle inclusions depends fundamentally on how the stress transfer from the ductile matrix to the stiff inclusions is described. Shear-lag models, as applied to geological systems (Ramberg, 1955; Hobbs, 1967; Lloyd et al., 1982; Pollard and Segall, 1987; Masuda and Kuriyama, 1988; Mandal et al., 1994; Ji and Saruwatari, 1998; Mandal et al., 2000) consider traction exerted by the flowing matrix

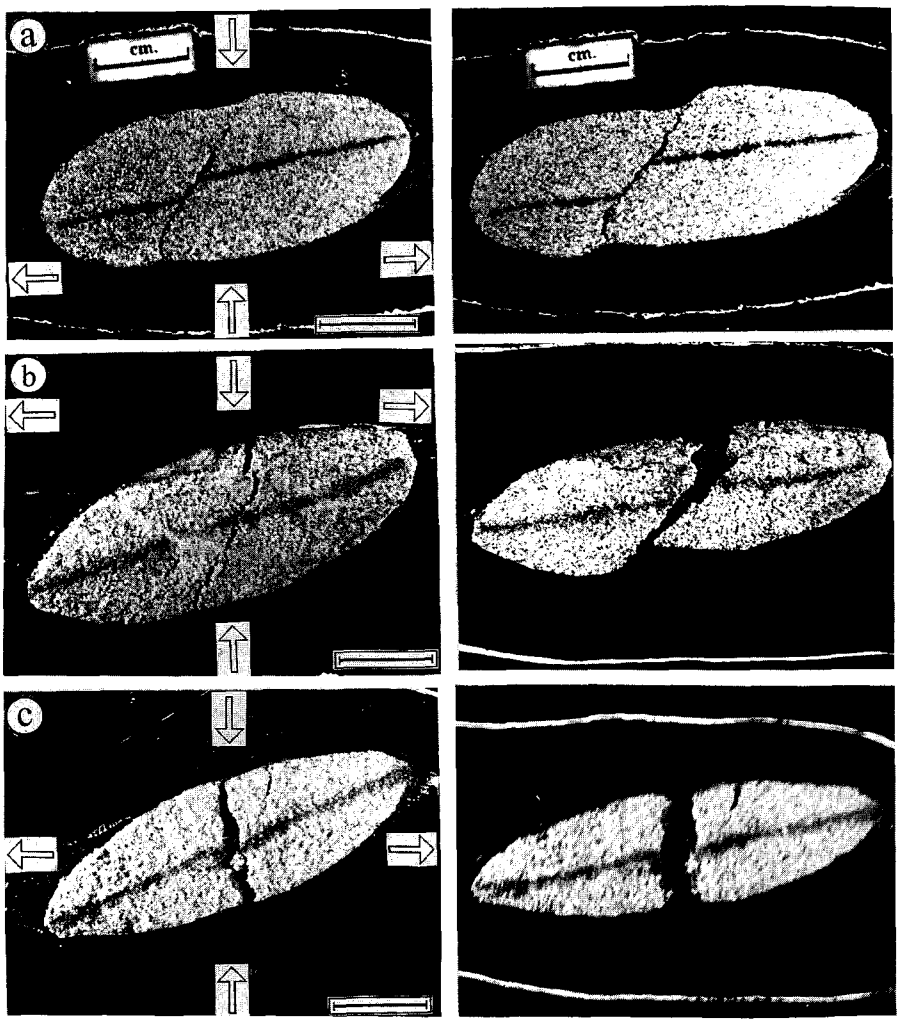

Fig. 4. Fracturing modes of obliquely oriented inclusions in the experiments during pure shear. Two successive stages of deformation are shown (left to right) (a) Mode 2a failure. (b) Mode 2b failure. (c) Mode 1 failure. The initial aspect ratios of the inclusions were 1.7, 2.4 and 3.4 respectively. The long axes of the inclusions were initially at an angle of 40° to the bulk extension direction. Scale bars = 2 cm.

onto the surface of the inclusion and determine the principal tensile stress within the inclusion by balancing the traction on either side of the principal section that lies at right angles to the long axis of the inclusion. When the principal tensile stress on that section exceeds the tensile strength, the inclusion develops tensile fracture along the section. Ramberg (1955) has shown that for rectangular inclusions experiencing axial tension, the maximum principal tensile stress acts on the central section of the inclusion and is oriented normal to its length producing tensile fractures passing through the inclusion's centre. Ji et al. (1997) analyzed development of tensile fractures within non-rectangular, ellipsoidal inclusions. They calculated the tensile stress within the inclusion by considering the traction over the entire surface of the inclusion as opposed to the Ramberg's model that considers the traction only along the long faces of a rectangular inclusion. This model shows that the initial fracture develops through mid-point fracturing at right angles to the long axis of the inclusion, but the subsequent fractures developing on the smaller, derivative fragments, do not necessarily form at their mid points.

The present model in addition to tensile fracture analyzes development of extensional shear and shear fractures within brittle inclusions hosted in an infinitely extended viscous medium as epitomized in the Griffith's criterion (cf. Hancock, 1985). However, in order to use Griffith's criterion in the analysis of failure mode it is necessary to calculate the principal tensile and compressive stresses within the inclusion. In the present analysis these stresses are calculated by considering traction components normal to and along a principal section. The principle of determining the stress within the inclusion from the surface traction is similar to that of Ji et al. (1997). However, to obtain the traction on the surface of the inclusion we have used the model developed by Jeffery (1922) describing the flow of a viscous medium around an ellipsoidal body.

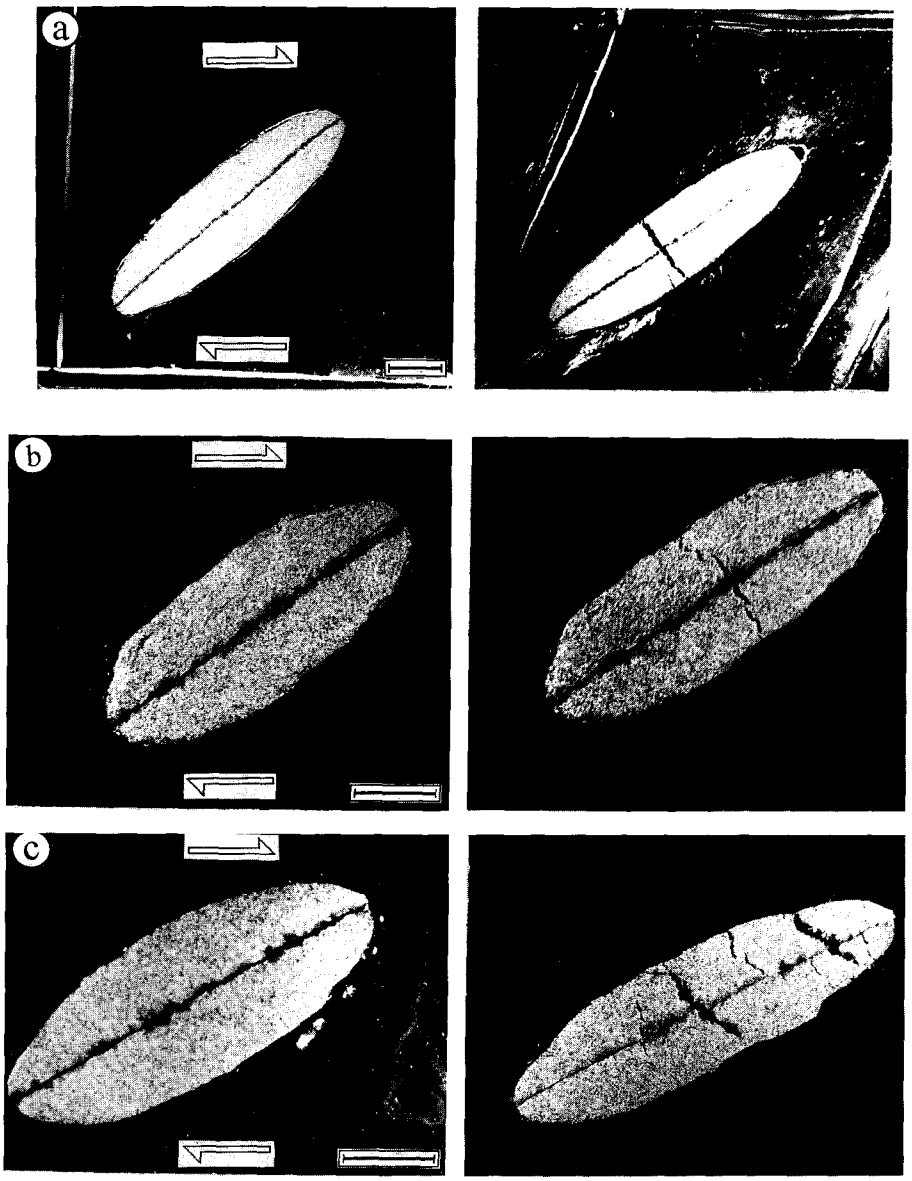

Fig. 5. Fracturing of the inclusions in the experiments during simple shear. (a) Mode 1 failure; the inclusion had an initial aspect ratio 4. (b) and (c) Mode 1 and Mode 2b failure; in both the models the inclusions had the same aspect ratio (2.6) but their initial orientations were 45° and 30° to the shear direction respectively. Scale bars = 2 cm.

3.1. Analysis of failure under pure shear

3.1.1. Inclusions with long axis parallel to the bulk extension direction

Consider an elliptical inclusion with semi-axes, a and b, within a viscous medium undergoing pure shear flow at a rate, $\dot{\varepsilon}$. A Cartesian reference, Oxy, is chosen with the origin at the centre of the inclusion, and with the x axis along the a axis of the inclusion (Fig. 6). The boundary of the inclusion can be represented as:

$$\frac{x^2}{a^2} + \frac{y^2}{b^2} = 1. \tag{1}$$

The viscous flow in the matrix will develop traction at the inclusion-matrix interface. At any point on the interface (Eq. (1)) the traction vector, T_s, is:

$$T_s = \begin{bmatrix} T_x \\ T_y \end{bmatrix} \tag{2}$$

where T_x and T_y are the traction components along the a and b axes of the inclusion which are given by:

$$T_x = P\left(L\frac{x}{a^2} + M\frac{y}{b^2}\right) \tag{3a}$$

$$T_y = P\left(M'\frac{x}{a^2} + L'\frac{y}{b^2}\right) \tag{3b}$$

where $\frac{1}{P^2} = \frac{x^2}{a^4} + \frac{y^2}{b^4}$ (Jeffery, 1922).

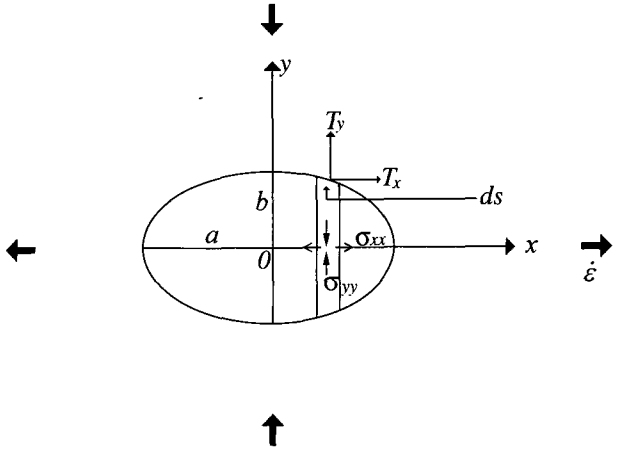

Fig. 6. The determination of the geometrical terms used in the theoretical analysis of the stress within an inclusion with its long axis parallel to the bulk extension direction during pure shear flow of the embedding medium. T_x and T_y are the components of the traction vector in the axial directions of the inclusion at any point (x, y) over a small surface area ds of the inclusion.

The constants in Eq. 3 can be shown to have the following expressions (see Eqs. (14), (A7) and (A9) in the appendix):

$$L = -p_o + 2\eta\dot{\varepsilon}(R+1)\cos 2\theta \tag{4a}$$

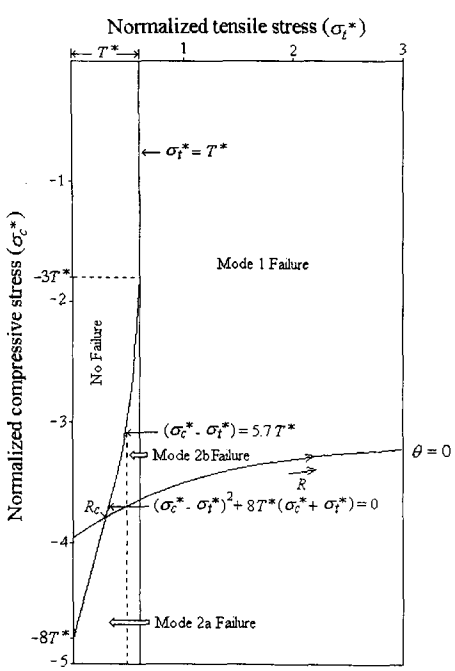

Fig. 7. Fields of different failure modes in the (σ_t^*, σ_c^*) space where σ_t^* and σ_c^* are the principal stresses in the inclusions as normalized by the bulk flow stress $(2\eta\dot{\varepsilon})$. The failure curve obtained from Griffith's failure criterion separates the stable (unshaded) and unstable (shaded) fields. The arrowed line shows the variation of principal tensile and compressive stresses within an inclusion with increasing aspect ratio (R). $\theta = 0$ signifies that the long axis of the inclusion is parallel to the bulk extension direction. The value of R at the point of intersection of the arrowed line with the failure curve represents the critical aspect ratio (R_c) for the commencement of fracturing within the inclusion.

$$L' = -p_o - 2\eta\dot{\varepsilon}\left(1 + \frac{1}{R}\right)\cos 2\theta \tag{4b}$$

$$M = -2\eta\dot{\varepsilon}\left[\frac{R+1}{R} + \frac{1}{R}\frac{R^2-1}{R^2+1}\right]\sin 2\theta \tag{4c}$$

$$M' = -2\eta\dot{\varepsilon}\left[(R+1) - R\frac{R^2-1}{R^2+1}\right]\sin 2\theta \tag{4d}$$

where $R = a/b$ and θ is the inclination of the long axis of the inclusion with respect to the bulk extension direction at any instant during the deformation. In this particular case, $\theta = 0$ and will remain so throughout the course of deformation. p_o and η are the confining pressure and the viscosity of the embedding medium respectively.

Stress equilibrium requires that the tensile stress σ_{xx} on a section at right angles to a-axis, located at a distance of x from the inclusion's centre be given by (Fig. 6):

$$-2y\sigma_{xx} + 2\int_x^a T_x ds = 0. \tag{5}$$

Replacing θ by 0 (since the long axis of the inclusion is parallel to the bulk extension direction in this case) in Eq. 4, we have, $M = M' = 0$. Eq. (3a) can then be written as:

$$T_x = \frac{a^2b^2}{\sqrt{b^4x^2 + a^4y^2}} L\frac{x}{a^2}. \tag{6}$$

The expression of ds in Eq. (5) is:

$$ds = \sqrt{1 + \left(\frac{dy}{dx}\right)^2}\, dx.$$

After differentiating Eq. (1) with respect to x, and then substituting (dy/dx),

$$ds = \frac{\sqrt{b^4x^2 + a^4y^2}}{a^2y} dx. \tag{7}$$

Replacing the expressions of T_x and ds in Eq. (5), we obtain

$$\sigma_{xx} = \frac{1}{y} L\frac{b}{a}\int_x^a \frac{x}{\sqrt{a^2 - x^2}} dx = L. \tag{8}$$

To find the compressive stress (σ_{yy}) along the section, we can write:

$$\sigma_{yy} = \frac{T_y ds}{dx} = L'. \tag{9}$$

Eqs. (8) and (9) give the principal tensile and compressive stresses along the axial directions of the inclusion which from Eqs. (4a) and (4b) can be expressed in terms of the axial ratio R of the inclusion as:

$$\sigma_t = -p_o + 2\eta\dot{\varepsilon}(1 + R) \tag{10a}$$

$$\sigma_c = -p_o - 2\eta\dot{\varepsilon}(1 + \frac{1}{R}). \tag{10b}$$

The above equations indicate that the stress inside an inclusion is homogeneous (cf. Eshelby, 1957), and dependent

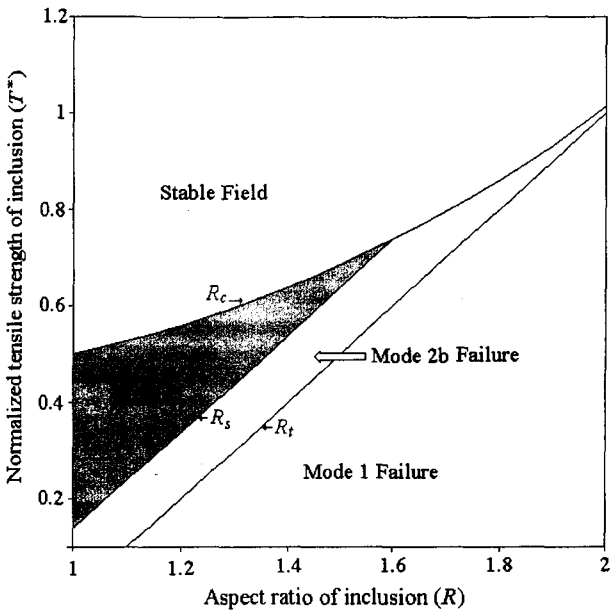

Fig. 8. Fields of different modes of fracturing in R-T^* space (at $p^* = 2$), where T^* is the tensile strength of inclusion normalized to the flow stress in the embedding medium. The curve marked R_c tracks the critical aspect ratios for brittle failure of inclusions of different tensile strengths. R_S and R_T are the critical aspect ratios defining the transitions between Mode 2a and Mode 2b, and between Mode 2 and Mode 1 fracturing respectively.

on the aspect ratio (R) of the inclusion at given p_o, η and $\dot{\varepsilon}$ values. The shape of the inclusion therefore appears to be a crucial parameter in controlling the fracturing modes, as seen in the experiments (Fig. 4).

The expressions of principal tensile and compressive stresses in Eq. 10 can now be utilized to analyze the failure of brittle inclusions using Griffith's criterion:

$$(\sigma_t - \sigma_c)^2 + 8T(\sigma_t + \sigma_c) = 0, \quad \text{if} \quad 3\sigma_t + \sigma_c < 0 \tag{11a}$$

$$\sigma_t = T \quad \text{if} \quad 3\sigma_t + \sigma_c > 0, \tag{11b}$$

(Jaeger, 1969), where T is the tensile strength of the inclusion.

Eq. (10) shows that the principal tensile stress increases linearly with R, whereas the principal compressive stress decreases asymptotically with increasing R. The curve describing the change in stress with increasing R of the inclusion in the (σ_t, σ_c) space meets the failure curve defined by Eq. (11) in that space at a point which represents the critical value of the aspect ratio for failure (Fig. 7). By substituting σ_t and σ_c of Eq. (10) in Eq. (11b), we can determine the critical aspect ratio (R_c) for failure as a function of relative tensile strengths of the inclusion and matrix $T^*(= T/2\eta\dot{\varepsilon})$ and the ratio between confining pressure and flow stress in the bulk deformation, $p^*(= p_0/2\eta\dot{\varepsilon})$ (Fig. 7). The critical aspect ratio as defined here is somewhat similar to the stable aspect ratio of layer-fragments that do not rupture further in the course of progressive deformation, as described previously by several workers (Ramberg, 1955; Lloyd et al., 1982; Kelly and MacMillan, 1986; Ji and Zhao, 1993; Wu and Pollard, 1995). This critical limit is, however, valid under the assumption that the stresses inside the inclusion are functions of the strain rate, as in Eq. (10), and do not increase with progressively increasing finite strain.

For a given relative tensile strength T^*, Mode 1 failure occurs when the aspect ratio is larger than R_t,

$$R_t = \left(\frac{T}{2\eta\dot{\varepsilon}}\right) + \left(\frac{p_o}{2\eta\dot{\varepsilon}}\right) - 1. \tag{12}$$

To rupture in Mode 2 satisfying the failure condition of Eq. (11a) the inclusions should have an aspect ratio less than R_t. The stress condition that marks the transition between Mode 2a and Mode 2b failure is given by:

$$\sigma_t - \sigma_c = 5.7T \tag{13}$$

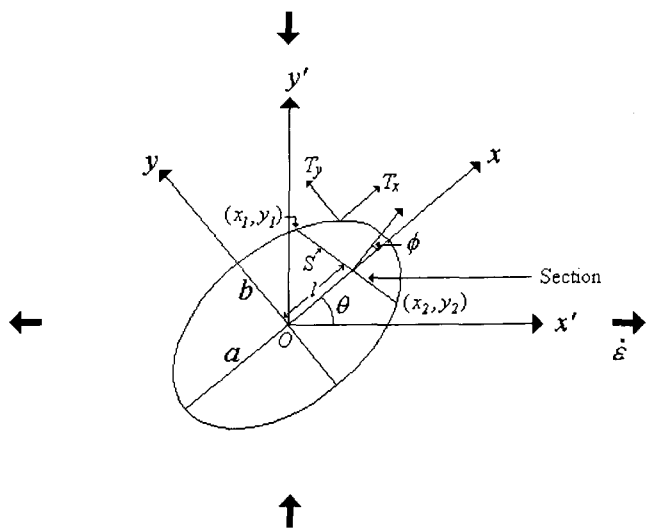

Fig. 9. The determination of the geometrical terms used in the analysis of the stresses within an obliquely oriented inclusion during pure shear deformation. S is an arbitrary section with its normal at angle ϕ with the long axis of the inclusion, and at a distance of l from the centre of the inclusion. The sectional line intersects the surface of the inclusion at points (x_1, y_1) and (x_2, y_2).

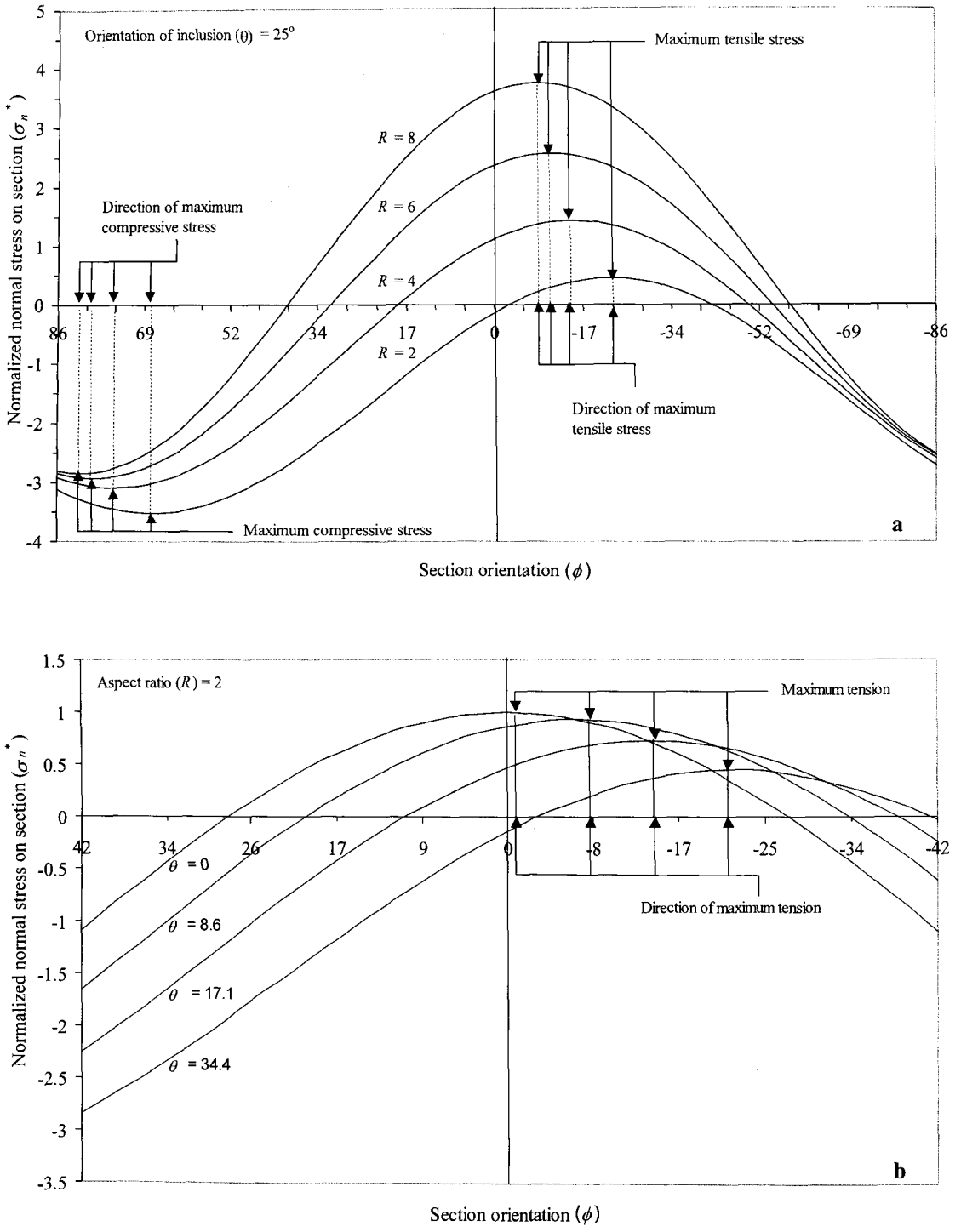

Fig. 10. Variation of the normal stress with section orientation (ϕ) contoured for different aspect ratios, R (a) and inclusion orientations, θ (b).

(Hancock, 1985). The critical aspect ratio that separates these two modes of fracturing can be obtained by substituting σ_t and σ_c from Eqs (10a) and (10b) in Eq. (13) (Fig. 8).

The failure map (Fig. 8) shows that: 1) the critical aspect ratio (R_c) for failure to occur increases nonlinearly with the relative tensile strength of the inclusion indicating that inclusions with higher relative tensile strength will require a greater aspect ratio to fracture under given conditions; 2) for very large tensile strength, failure is possible only by Mode 1 tensile fracturing; and 3) for a particular tensile strength, Mode 1 failure is successively followed by Mode 2b and Mode 2a with decreasing aspect ratio of inclusions.

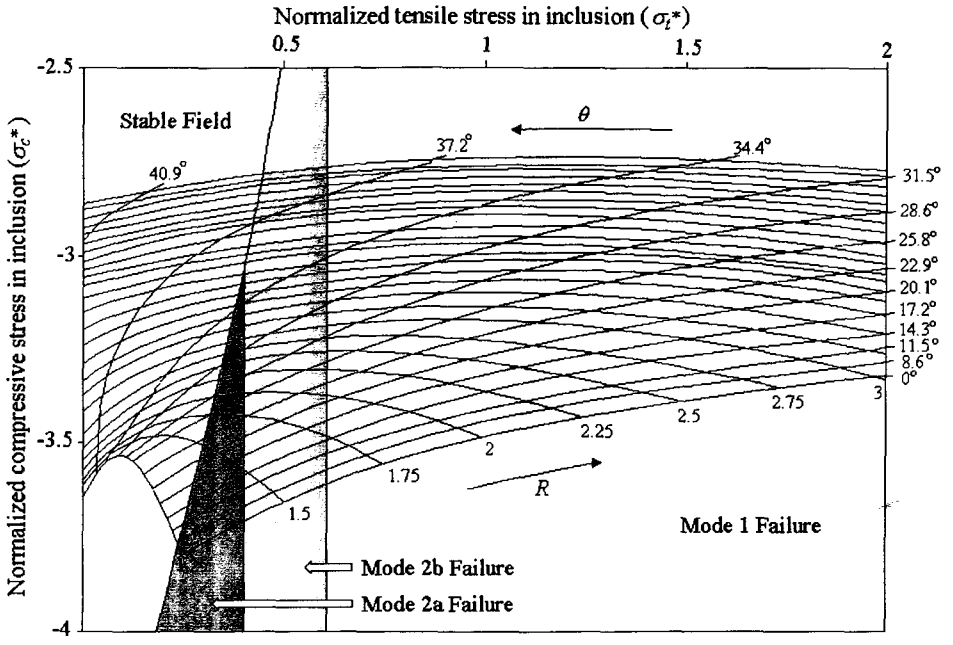

Fig. 11. Plots of the principal tensile and compressive stresses within inclusions in the (σ_t^*, σ_c^*) space. Contoured for R at constant θ, and θ at constant R. The stable and unstable fields as shown in Fig. 7 are superimposed. $p^* = 2$.

3.1.2. Inclusions with long axis oblique to the bulk extension direction

Experimental results, discussed in Section 2.2 indicated that inclusion orientation is an additional factor in controlling the fracturing of the inclusions. In order to determine the orientation, at which fracture develops within an inclusion and also the influence of the orientation on fracture mode, we need to consider a general case where the long axis of the inclusion is oblique to the bulk extension direction. Also, the stress within the inclusion needs to be determined on arbitrarily oriented sections. Let the long axis of the inclusion at an instant of progressive deformation be at an angle of θ to the bulk extension direction. In addition to Oxy, we take another co-ordinate frame, $Ox'y'$, with origin at the inclusion centre, with the x' axis parallel to the bulk extension direction (Fig. 9). If the bulk extension rate is $\dot{\varepsilon}$ along x' direction, the strain-rate (S_{ij}) and rotation-rate (S_w) components with reference to Oxy are as follows:

$$S_{11} = \dot{\varepsilon}\cos 2\theta, \quad S_{22} = -\dot{\varepsilon}\cos 2\theta$$
$$S_{12} = -\dot{\varepsilon}\sin 2\theta \quad S_w = 0. \tag{14}$$

Let us consider an oblique section at a distance, l, from the centre of the inclusion. The section-normal is at an angle ϕ with the long axis of the inclusion (Fig. 9). The section line intersects the boundary of the inclusion at points, (x_1, y_1) and (x_2, y_2). The normal stress (σ_n) on this section can be obtained from Eq. (3) between the limits x_1 and x_2:

$$-2S\sigma_n + 2\int_{x_1}^{x_2} T_n ds = 0 \tag{15}$$

where, $T_n = T_x\cos\phi + T_y\sin\phi$, and S is the section length. The solution of this equation is:

$$\sigma_n.S = \frac{1}{R}\Big[(L\cos\phi - M'\sin\phi)\sqrt{a^2 - x_1^2} + (L\cos\phi + M'\sin\phi)\sqrt{a^2 - x_2^2}\Big] + [(M'\cos\phi - L\sin\phi)(a - x_1) + (L'\sin\phi - M\cos\phi)(a - x_2)]. \tag{16}$$

The expressions for L, M, L' and M' are given in Eq. (4). The integration limits, x_1 and x_2, and the section length, S, in Eq. (16) can be determined in terms of the distance of the section from inclusion's centre (l) and the orientation of the section (ϕ) as:

$$x_1 = \frac{1 - \sqrt{1 - \left(1 + \frac{m^2}{R^2}\right)\left(1 - \frac{m^2}{R^2}\frac{a^2}{l^2}\right)}}{1 + \frac{m^2}{R^2}}\, l,$$

$$x_2 = \frac{1 + \sqrt{1 - \left(1 + \frac{m^2}{R^2}\right)\left(1 - \frac{m^2}{R^2}\frac{a^2}{l^2}\right)}}{1 + \frac{m^2}{R^2}}\, l,$$

$$S = 2R\left(\frac{m^2 + 1}{m^2 + R^2}\right)^{\frac{1}{2}}\left(\frac{a^2}{R^2} - \frac{1}{m^2 + R^2}l^2\right)^{\frac{1}{2}}$$

where $m = \tan\phi$.

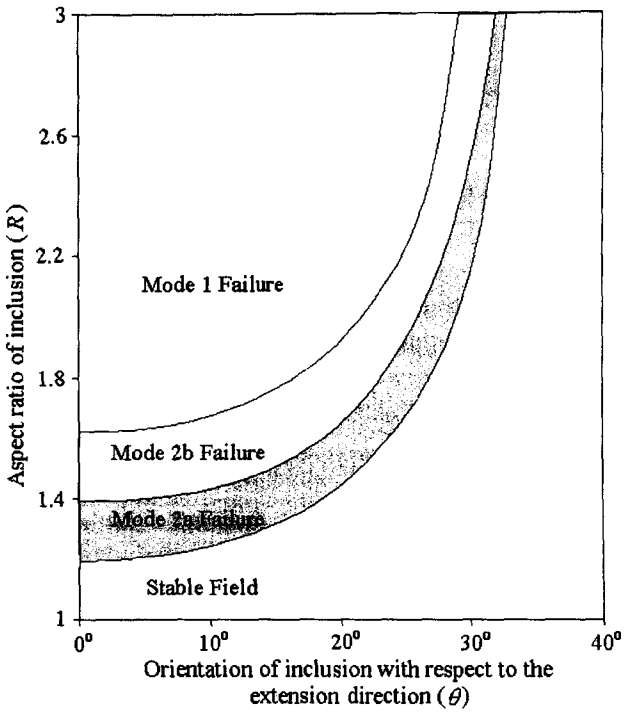

Fig. 12. Fields for the three modes of failure (under pure shear) in the R-θ space.

For a given aspect ratio (R) and inclusion orientation (θ), the normal stress on the section varies with orientation (ϕ). In Fig. (10a) the dependence of σ_n on R, θ and ϕ, as given by Eq. (16) is shown. The normal stress becomes a maximum and a minimum on two orthogonal sections each with a specific value of ϕ at a particular R and θ. The stresses on these sections correspond to the principal tensile and compressive stresses within the inclusion and the section normals represent the principal axes of stress (Fig. 10a).

The orientations of the principal axes of stress within the inclusion appear to vary with the aspect ratio (R) and inclusion orientation (θ). At low values of R the principal tensile stress is oriented at an angle to the long axis of the inclusion. This angle decreases with increasing R (Fig. 10a) and increases with increasing θ (Fig. 10b). This implies that Mode 1 fractures in obliquely oriented inclusions need not necessarily be at right angles to the long axis of the inclusions, as also seen in the experiments. Indeed they form nearly at right angles to the long axis of the inclusions only when the aspect ratio of the inclusion is very large (>3.5) or the inclusion orientation at which fractures develop is close to the bulk extension direction.

The maximum tensile and compressive stresses in inclusions oriented obliquely to the bulk extension direction during pure shear (as determined from Eq. (16)) are shown contoured for inclusion orientation and aspect ratio in Fig. 11. The geometric conditions leading to the different modes of failure of such inclusions may be deduced by superimposing the field diagrams of different failure modes (Fig. 7) onto this plot. The values of aspect ratios and inclusion orientations at which failure occurs are then plotted in R-θ space in Fig. 12. The plot shows that inclusions with aspect ratio below a critical value (in the present case 1.2) do not fracture at any orientation. Similarly, inclusions of any aspect ratio remain stable until they are oriented at angles greater than 35° to the bulk extension direction. Mode 1 failure covers a large area in the failure field and occurs above an aspect ratio of 1.6 and at an inclusion orientation of less than 30°. The field of Mode 1 fracturing progressively widens with increasing aspect ratio in contrast to those of Mode 2a and Mode 2b that become narrower as the aspect ratio is increased, with the field of Mode 2a narrowing down more rapidly than that of Mode 2b.

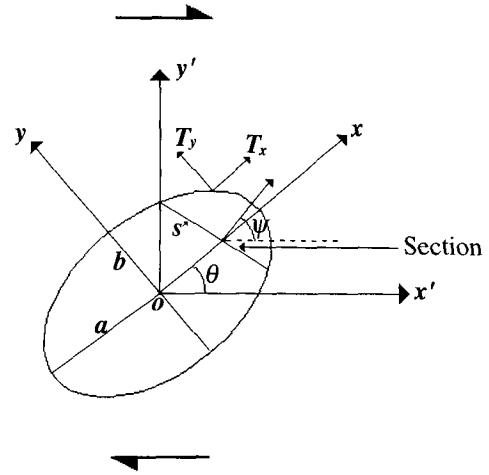

Fig. 13. The determination of the geometric terms used in the analysis of the stresses within an obliquely oriented inclusion during simple shear.

3.2. Analysis of failure in simple shear

Consider an inclusion with semi-axes, a and b within a viscous medium undergoing shear at a rate, $\dot{\gamma}$; the long axis of the inclusion is at an angle θ with the shear direction (Fig. 13). The reference frame Oxy is fixed to the inclusion at its centre, with the x axis along the a axis. Another reference frame, $Ox'y'$ with its origin at the inclusion centre is defined with the x' axis along the shear direction (Fig. 13). If the bulk shear rate is $\dot{\gamma}$ along x' axis, the strain-rate components with reference to Oxy are as follows:

$$S_{11} = \frac{1}{2}\dot{\gamma}\sin 2\theta,\quad S_{22} = -\frac{1}{2}\dot{\gamma}\sin 2\theta,\quad S_{12} = \frac{1}{2}\dot{\gamma}\cos 2\theta \text{ and } S_w = -\frac{\dot{\gamma}}{2}.$$

These strain-rate components are used for obtaining the constants in the velocity functions, as given in Eq. (A7). The expressions of L, L', M, M' in the function of traction vector (Eq. (2)) for simple shear deformation are then derived from

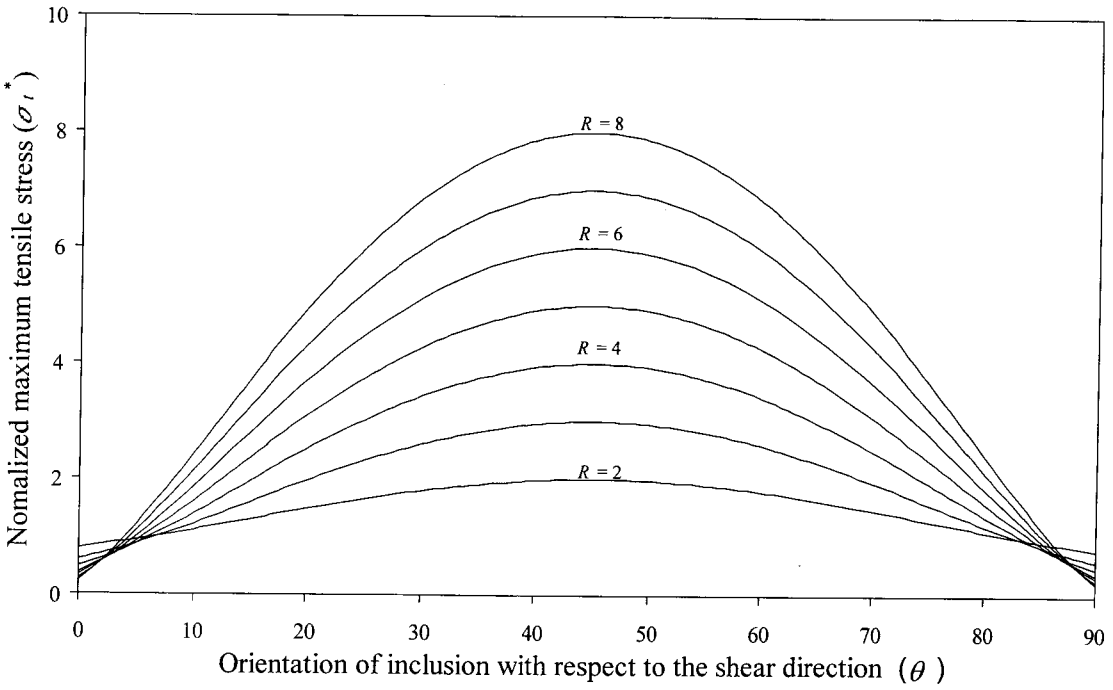

Fig. 14. Plots of principal tensile stress versus inclusion orientation with respect to the shear direction (θ) for different values of the aspect ratio (R).

Eqs. (A7) and (A9) as:

$$L = -p_o + \eta\dot{\gamma}(1 + R)\sin 2\theta \tag{17a}$$

$$L' = -p_o - \eta\dot{\gamma}(1 + \frac{1}{R})\sin 2\theta \tag{17b}$$

$$M = \eta\dot{\gamma}\left[\frac{R+1}{R}\cos 2\theta - \frac{1}{R}(1 + 2\frac{R^2\sin^2\theta + \cos^2\theta}{R^2+1})\right] \tag{17c}$$

$$M' = \eta\dot{\gamma}\left[(R+1)\cos 2\theta + R\left(1 + 2\frac{R^2\sin^2\theta + \cos^2\theta}{R^2+1}\right)\right]. \tag{17d}$$

Consider an oblique section within the inclusion with its normal at an angle ψ with the shear direction. Following the same method as in the case of pure shear deformation, the magnitudes of principal tensile and compressive stresses and their orientations (represented by ψ values of the corresponding sections) within the inclusion may be determined, for different inclusion orientations (θ) at different values of aspect ratio (R) (Figs. 14 and 15).

The principal tensile stress within the inclusion attains a maximum value when the inclusion orientation is 45° irrespective of the aspect ratio (Fig. 14). The magnitude of the principal tensile stress increases with increasing R except when the inclusion orientation is nearly parallel or perpendicular to the shear direction (Fig. 14). The orientation of the principal axis of tensile stress changes with inclusion orientation in sinusoidal fashion for all values of R (Fig. 15). The principal axis of tension within the inclusion is at an angle of 45° with the shear direction when the inclusion orientation (θ) is 0°, 45° and 90° with respect to the shear direction (Fig. 15).

Fig. 16 shows the variations of the principal tensile and compressive stresses in (σ_t, σ_c) space contoured as a function of R and θ. The aspect ratios and inclusion orientations that satisfy the failure criterion in Eq. (11) can be found by superimposing the field diagram of different failure modes (Fig. 7) on Fig. 16. The values of aspect ratios and inclusion orientations so obtained are plotted in R-θ space (Fig. 17). Inclusions with an aspect ratio less than 1.2 will not fracture at all (Fig. 17) at any orientation they may define during the course of deformation. Again, fracture will not develop in inclusions when they are oriented at angles less than 10° or greater than 80° with the shear direction. The failure field indicates that Mode 1 fracturing takes place for wide ranges of aspect ratio and inclusion orientation above an aspect ratio of 1.6. As in the case of pure shear, the fields of Mode 2a and Mode 2b fracturing progressively narrow with increasing aspect ratio (Fig. 17).

4. Conclusions

The outcome of the present analysis can be summarized along the following points.

1. Brittle inclusions deforming in a ductile matrix can fail in any of three modes: tensile fracturing (Mode 1), shear fracturing (Mode 2a) and extensional shear fracturing (Mode 2b). At given confining pressure and bulk strain rate of a system, the mode of deformation is primarily

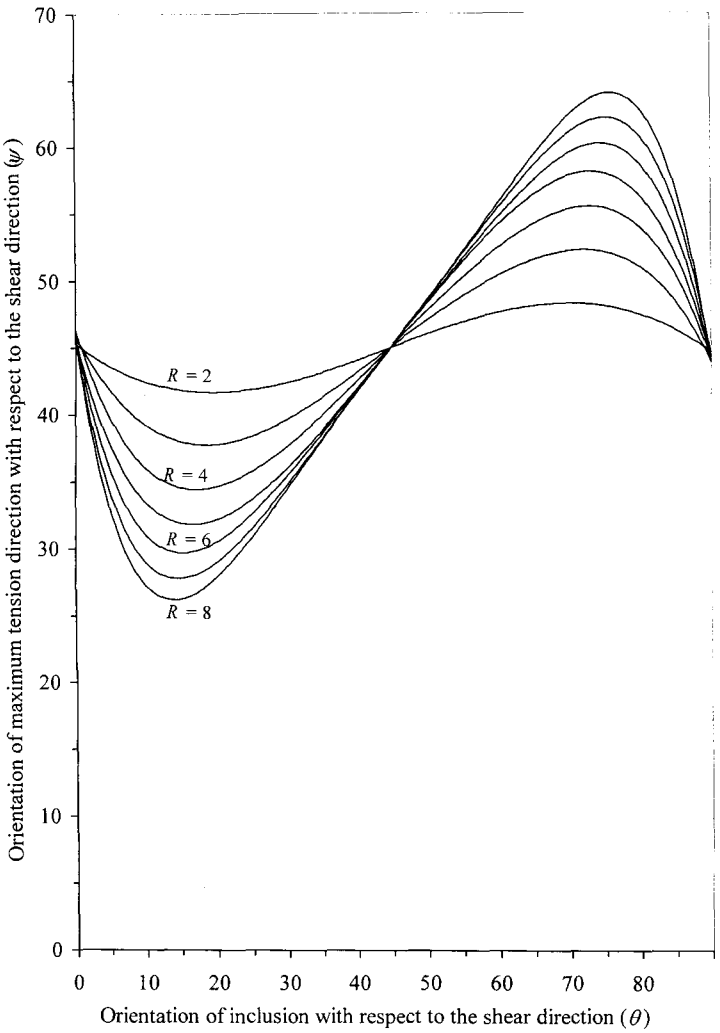

Fig. 15. Plots of the principal tension direction versus inclusion orientation with respect to the shear direction for different values of aspect ratio (R).

controlled by the tensile strength, aspect ratio and instantaneous orientation of the inclusion. Inclusions with higher tensile strength require a larger aspect ratio to fracture at given conditions in pure shear deformation. Where the failure criterion is met, Mode 1 failure is possible for low relative tensile strength or high aspect ratio; Mode 2a failure is favoured at low aspect ratios and low tensile strength, and Mode 2b failure is favoured at intermediate values of tensile strength and aspect ratio. Mode 1 failure is favoured when the inclusions have large aspect ratios and their long axes are at angles less than 30° to the bulk extension direction in pure shear, and at angles between 15° to 75° to the shear direction in simple shear during progressive deformation. Mode 2a failure is favoured by low aspect ratio or when the inclusion is oriented at high angle to the maximum extension direction, and is replaced by Mode 2b for larger aspect ratios.

2. The principal tensile stress is directly proportional to the ellipticity of the inclusion, whereas the principal compressive stress is inversely proportional to the ellipticity, so that with decreasing ellipticity, Mode 1 failure is replaced by Mode 2b and finally by Mode 2a, for inclusions with an orientation that is conducive for all the modes of fracturing. Inclusions with axial ratio less than a critical value do not fracture, and remain stable in progressive deformation.
3. Mode 1 fractures in obliquely oriented inclusions are not necessarily at right angles to the long axis of the inclusions, as observed in experiments. They form approximately at right angles to the long axis of the inclusions only when the aspect ratio of the inclusion is very large or the inclusion orientation at the moment of fracturing is close to the bulk extension direction. Mode 1 fractures in simple shear make an angle close to 135° with the shear direction only when the aspect ratio of inclusions is low or if the long axis of the inclusion is initially at an angle of 45° to the shear direction. In other situations the

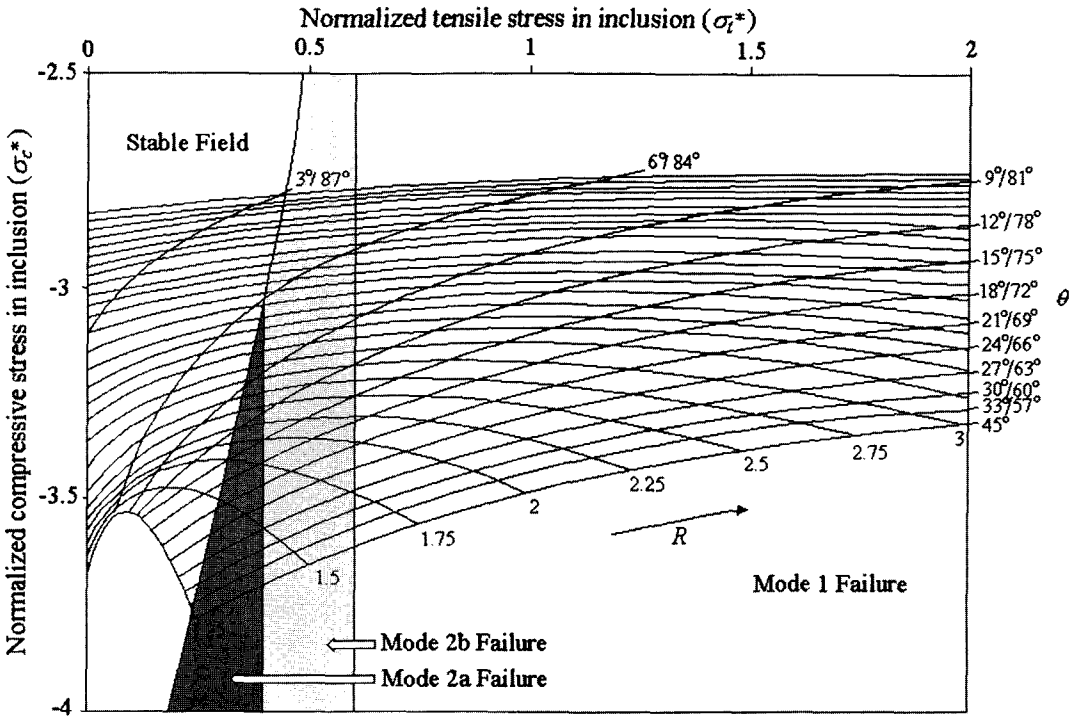

Fig. 16. Plots of principal tensile and compressive stresses within an inclusion in the (σ_t^*, σ_c^*) space during simple shear deformation (see the caption of Fig. 11 for the methodology). R and θ are the aspect ratio and inclusion orientation with respect to the shear direction respectively. $p^* = 2$.

inclination of the Mode 1 fractures deviates from 135° but remains within a range (Fig. 15) that increases with increasing aspect ratio.

4. There are a number of limitations in our theoretical model. (i) The model assumes that there is a perfect coupling between the inclusion and the embedding ductile matrix. However, the degree of coupling would be an additional factor in controlling the stresses inside

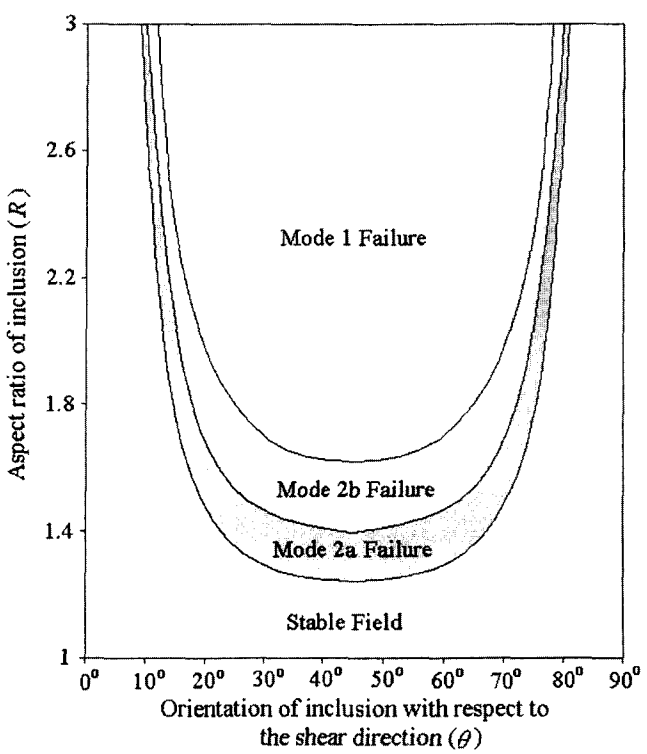

Fig. 17. Fields for the three modes of failure during simple shear in the R-θ space.

the inclusion (cf. Kenkmann and Dresen, 1998) and thereby the mode of fracturing of the inclusion. (ii) The inclusion is considered to be ideally brittle, and does not undergo any ductile deformation. (iii) The embedding medium is assumed to be Newtonian viscous. (iv) The analysis is two-dimensional, and assumes that the inclusions float in an infinitely extended medium, and are mutually non-interacting. (v) The results presented in this paper are applicable to systems that undergo deformation under pure- or simple-shear stresses, and therefore may not tally with results obtained from the deformations of fibre composites under uniaxial tension. Due to these limitations, the different critical values of aspect ratio and inclusion orientations mentioned in the paper for different modes of failure are strictly relative in nature and may not exactly match natural data and experimental results presented here.

Acknowledgements

We wish to thank Drs S. Covey-Crump and G. Dresen for reviewing the manuscript critically and suggesting many improvements. We also thank Dr J. Turner for giving us a guideline for revising the manuscript. The present work was carried out under a project of DST, India, sanctioned to NM. CC acknowledges the infrastructural facilities provided by the Indian Statistical Institute, Calcutta. Abhradip Das is specially thanked for his help in the experiments.

Appendix A

In this section we present a two-dimensional mathematical approach in formulating the traction exerted by a ductile medium on the surface of a rigid inclusion embedded within it. Consider an inclusion, with semi-axes a and b, floating in an infinitely extended viscous medium of viscosity η. A reference frame is chosen with an origin at the centre of the inclusion with x axis along a axis (Fig. 1). With respect to Oxy, the far-field flow in the embedding medium is represented by:

$$u_0 = S_{11}x + S_{12}y - S_w y \tag{A1a}$$

$$v_0 = S_{12}x + S_{22}y + S_w x \tag{A1b}$$

where S_{ij} and S_w are distortion and rotation rate tensors with respect to Oxy. The traction on the surface of the inclusion can be determined from the theory of the flow of a viscous medium around an ellipsoidal rigid body developed by Jeffery (1922). The present analysis is, however, made in two-dimensions. It is convenient to use curvilinear coordinates:

$$\frac{x^2}{a^2+\lambda} + \frac{y^2}{b^2+\lambda} = 1 \tag{A2}$$

where $\lambda = 0$ is the boundary of the inclusion. To derive the velocity field in the embedding medium around the inclusion one requires knowledge of the variables, α, β, and γ, where:

$$\alpha = \int_\lambda^\infty \frac{d\lambda}{(a^2+\lambda)\Delta}, \qquad \beta = \int_\lambda^\infty \frac{d\lambda}{(a^2+\lambda)\Delta} \qquad \text{and}$$
$$\gamma = \int_\lambda^\infty \frac{d\lambda}{(a^2+\lambda)(b^2+\lambda)\Delta} \tag{A3}$$

where $\Delta = [(a^2+\lambda)(b^2+\lambda)]^{1/2}$. In formulating the velocity field around the inclusion it is necessary to impose boundary conditions for $\lambda = 0$ (Jeffery, 1922), from which the expression of the terms in Eq. (A3) are determined in the following way.

Defining

$$\alpha_o = \int_o^\infty \frac{d\lambda}{(a^2+\lambda)\Delta}.$$

We substitute $Z = (b^2+\lambda)^{1/2}$ and have,

$$\alpha_o = \int_b^\infty \frac{d\lambda}{(Z^2+A^2)^{3/2}},$$

where $A^2 = a^2 - b^2$. Substituting $Z = A\tan\theta$ and get,

$$\alpha_o = \frac{2}{A^2}\int_{\tan^{-1}b/A}^{\frac{\pi}{2}} \cos\theta d\theta = \frac{2}{a(a+b)}.$$

Following the same method, we get:

$$\beta_o = \frac{2}{b(a+b)} \qquad \text{and} \qquad \gamma_o = \frac{2}{ab(a+b)^2}.$$

After Equations (22) and (23) of Jeffery (1922), we can write the velocity components at a point in the neighborhood of an ellipsoidal inclusion in two dimensions:

$$u = \left[S_{11} + W\gamma - 2A\left(\alpha+\beta\right)\right]x + \left[S_{12} - S_w + T\gamma + 2\left(\alpha H' - \beta H\right)\right]y - \frac{2xyP^2}{\Delta^3}\left[\left\{T + 2\left(a^2+\lambda\right)H + 2\left(b^2+\lambda\right)H'\right\}\frac{x}{\left(a^2+\lambda\right)} + \left\{W - 2\left(a^2+\lambda\right)A + 2\left(b^2+\lambda\right)B\right\}\frac{y}{\left(b^2+\lambda\right)}\right] \tag{A4a}$$

$$v = \left[S_{11} + S_w + T\gamma - 2\left(\alpha H' + \beta H\right)\right]x + \left[S_{12} - W\gamma - 2B\left(\alpha + \beta\right)\right]y - \frac{2xyP^2}{\Delta^3}\left[\left\{T + 2\left(a^2 + \lambda\right)H + 2\left(b^2 + \lambda\right)H'\right\} \times \frac{y}{\left(b^2 + \lambda\right)} - \left\{W - 2\left(a^2 + \lambda\right)A + 2\left(b^2 + \lambda\right)B\right\}\frac{x}{\left(a^2 + \lambda\right)}\right]. \quad \text{(A4b)}$$

Let the inclusion be assumed free to rotate at a velocity, ω. Then the velocity of a point on the surface of inclusion ($\lambda = 0$) is,

$$u_s = -\omega y, \quad \text{and} \quad v_s = \omega x. \quad \text{(A5)}$$

Replacing λ by 0 in Eqs. (A4a) and (A4b) and comparing them with Eq. (A5), we have following relations:

$$S_{11} + W\gamma - 2A(\alpha_o + \beta_o) = 0 \quad \text{(A6a)}$$

$$S_{12} - S_w + T\gamma + 2(\alpha_o H' - \beta_o H) = -\omega \quad \text{(A6b)}$$

$$T + 2a^2H + 2b^2H' = 0 \quad \text{(A6c)}$$

$$W - 2a^2A + 2b^2B = 0 \quad \text{(A6d)}$$

$$S_{12} + S_w + T\gamma_o - 2(\alpha_o H' - \beta_o H) = \omega \quad \text{(A6e)}$$

$$S_{22} - W\gamma_o - 2B(\alpha_o + \beta_o) = 0. \quad \text{(A6f)}$$

Now, solving five Eqs. (A6 a–f) we obtain the constants in Eq. (A4) in term of known quantities:

$$A = \frac{S_{11}}{2[(\alpha_o + \beta_o) - (a^2 + b^2)\gamma_o]},$$

$$B = -\frac{S_{11}}{2[(\alpha_o + \beta_o) - (a^2 + b^2)\gamma_o]},$$

$$H = \frac{\alpha_o S_{12} - \gamma_o b^2(S_w - \omega)}{2(\alpha_o a^2 + \beta_o b^2)\gamma_o},$$

$$H' = \frac{\beta_o S_{12} + \gamma_o a^2(S_w - \omega)}{2(\alpha_o a^2 + \beta_o b^2)\gamma_o}, \quad \text{(A7)}$$

$$T = -\frac{S_{12}}{\gamma_o},$$

$$W = \frac{S_{11}(a^2 + b^2)}{(\alpha_o + \beta_o) - (a^2 + b^2)\gamma_o},$$

where,

$$\omega = \frac{a^2(S_w + S_{12}) + b^2(S_w - S_{12})}{a^2 + b^2}$$

(Eq. 39 of Jeffery, 1922).

The flow in the embedding medium, described by Eq. (A4), develops traction at the interface between the inclusion and the embedding medium. Considering a plane strain condition, the traction components at any point on the surface of the inclusion can be written (cf. Eq. 34 of Jeffery, 1922):

$$T_x = P\left(L\frac{x}{a^2} + M\frac{y}{b^2}\right) \quad \text{(A8a)}$$

$$T_y = P\left(M'\frac{x}{a^2} + L'\frac{y}{b^2}\right), \quad \text{(A8b)}$$

where,

$$\frac{1}{P^2} = \frac{x^2}{a^4} + \frac{y^2}{b^4}$$

and

$$L = -p_0 + 4\eta\left\{\frac{2}{ab} - (\alpha_0 - \beta_0)\right\}A \quad \text{(A9a)}$$

$$M = \frac{8\eta}{ab}H \quad \text{(A9b)}$$

$$L' = -p_0 - 4\eta\left\{\frac{2}{ab} + (\alpha_0 - \beta_0)\right\}A \quad \text{(A9c)}$$

$$M' = \frac{8\eta}{ab}H' \quad \text{(A9d)}$$

p_o and η are the confining pressure and coefficient of viscosity of the matrix respectively.

References

Cox, H.L., 1952. The elasticity and strength of paper and other fibrous materials. British Journal of Applied Physics 3, 72–79.

Eshelby, J.D., 1957. The determination of the elastic field of an ellipsoidal inclusion and related problems. Proceedings of the Royal Society of London A241, 376–396.

Hancock, P.L., 1985. Brittle microtectonics: principles and practices. Journal of Structural Geology 7, 437–457.

Hippertt, J.F.N., 1993. V-pull apart microstructures: a new shear sense indicator. Journal of Structural Geology 15, 1393–1404.

Hobbs, D.W., 1967. The formation of tension joints in sedimentary rocks: an explanation. Geological Magazine 104, 550–556.

Huiqi, L., McClay, K.R., Powell, D., 1992. Physical models of thrust wedges. In: McClay, K.R (Ed.), Thrust Tectonics, Chapman and Hall, London.

Jaeger, J.C., 1969. Elasticity, Fracture and Flow. Methuen, London.

Jeffery, G.B., 1922. The motion of ellipsoidal particles immersed in a viscous fluid. Proceedings of the Royal Society of London A 120, 161–179.

Ji, S., Saruwatari, K., 1998. A revised model for the relationship between

joint spacing and layer thickness. Journal of Structural Geology 20, 1495–1508.

Ji, S., Zhao, P., 1993. Location of tensile fracture within rigid-brittle inclusions in ductile flowing matrix. Tectonophysics 220, 23–31.

Ji, S., Zhao, P., Saruwatari, K., 1997. Fracturing of garnet crystals in anisotropic rocks during uplift. Journal of Structural Geology 19, 603–620.

Kelly, A., MacMillan, N.H., 1986. Strong Solids. Oxford Science Publications, Oxford.

Kenkmann, T., Dresen, G., 1998. Stress gradients around porphyroclasts: palaeopiezometric estimates and numerical modelling. Journal of Structural Geology 20, 163–173.

Lloyd, G.E., Ferguson, C.C., 1981. Boudinage structure-some new interpretations based on elastic-plastic finite element simulations. Journal of Structural Geology 3, 117–129.

Lloyd, G.E., Ferguson, C.C., Reading, K., 1982. A stress-transfer model for the development of extension fracture boudinage. Journal of Structural Geology 4, 355–372.

Mandal, N., Chakraborty, C., Samanta, S.K., 2000. Boudinage in multilayered rocks under layer-normal compression: a theoretical analysis. Journal of Structural Geology 22, 373–382.

Mandal, N., Chattopadhyay, A., Bose, S., 1997. Imbricate thrust spacing: experimental and theoretical analysis. In: Sengupta, S (Ed.), Evolution of structures: micro- to macro-scale, Chapman & Hall, London, pp. 143–165.

Mandal, N., Deb, S.K., Khan, D., 1994. Evidence of a non-linear relationship between fracture spacing and layer thickness. Journal of Structural Geology 16, 1275–1281.

Masuda, T., Kuriyama, M., 1988. Successive "mid-point" fracturing during microboudinage: an estimate of the stress – strain relation during a natural deformation. Tectonophysics 147, 171–177.

McClay, K.R., Ellis, P.G., 1987. Geometries of extensional fault systems developed in model experiments. Geology 15, 341–344.

Michibayashi, K., 1996. The role of intragranular fracturing on grain size reduction in feldspar during mylonitization. Journal of Structural Geology 18, 17–25.

Mitra, S., 1978. Microscopic deformation mechanisms and flow laws in quartzites within the South Mountain anticline. Journal of Geology 86, 129–152.

Mulugeta, G., 1988. Modelling the geometry of Coulomb thrust wedges. Journal of Structural Geology 10, 847–859.

Pollard, D.D., Segall, P., 1987. Theoretical displacements and stresses near fractures in rocks with applications to faults, joints, veins, dikes, and solution surfaces. In: Atkinson, B.K. (Ed.), Fracture Mechanics of Rocks, Academic Press, London.

Ramberg, H., 1955. Natural and experimental boudinage and pinch-and swell structures. Journal of Geology 63, 512–526.

Ramsay, J.G., Huber, M.I., 1987. The Techniques of Modern Structural Geology, Folds and Fractures, 2. Academic Press, London, pp. 309–700.

Wu, H., Pollard, D.D., 1995. An experimental study of the relationship between joint spacing and layer thickness. Journal of Structural Geology 17, 887–905.